Acta Polytechnica CTU Proceedings **48**:34–40, 2024
https://doi.org/10.14311/APP.2024.48.0034

© 2024 The Author(s). Licensed under a CC-BY 4.0 licence

Published by the Czech Technical University in Prague

TRIBO-TECHNOLOGICAL FEATURES OF LASER POWDER BED FUSION PROCESS: SCRATCH AND WEAR RESISTANCE OF ALSI$_{10}$MG ALUMINIUM ALLOY

Danilo Guarino, Simone Venettacci*, Vittorio Villani,
Gennaro Salvatore Ponticelli, Stefano Guarino

Università degli Studi Niccolò Cusano, Roma, Via Don Carlo Gnocchi, 3, Italy

* corresponding author: simone.venettacci@unicusano.it

Abstract. Mechanical systems, regardless of their complexity, very often require that different parts must move relative to each other by sliding their surfaces, therefore appropriate tribological properties are needed. This request appears particularly evident for components fabricated through Metal Additive Manufacturing processes, due to their typical high surface roughness. In the current study, the Laser Powder Bed Fusion technique with optimized parameters is used to produce samples made of AlSi$_{10}$Mg alloy. Their tribo-technological properties are investigated through progressive load scratch and dry ball-on-plate wear tests. Along with a global characterization, a local analysis has been performed to identify any variations induced by the building direction. The friction coefficient and the wear rate are generally higher than as-cast specimens. Finally, local trends suggest that the central parts of the samples average offer higher resistance to wear and scratch than the outer areas.

Keywords: Laser powder bed fusion, tribology, scratch test.

1. Introduction

The present work deals with an investigation of tribo-technological features of AlSi$_{10}$Mg components made by Laser Powder Bed Fusion (LPBF) [1]. This technique belongs to the innovative Metal Additive Manufacturing (MAM) technologies for the production of mechanical components and rapid prototyping [2]. Starting from the geometry of a three-dimensional digital model, it is possible to generate an object even with a complex shape and high level of customization by simple overlapping of material layers [3]. Compared to traditional technologies (such as casting, forging, etc.), MAM ones offer the possibility to optimize the structure of the component, reduce processing waste, reduce time and costs for small series productions [4, 5], while also ensuring higher levels of production flexibility, greater sustainability and ease of innovation. On the contrary, the lack of knowledge and standardization, as well as the material anisotropy, and high surface roughness represent the main current limitations to the use of this technology in the industrial sectors [6]. In this area, it has already been verified how poor surface finish can be one of the main critical issues of mechanical parts produced by Additive Manufacturing (AM), going to compromise their reliability in service [7]. Increased performance can be achieved through various post-processing techniques [8], which, however, have proven to be difficult or unaffordable for complex geometries, as well as limiting in terms of manufacturing flexibility and finished product design, in addition to raising production time and cost [9].

The aluminum AlSi$_{10}$Mg alloy analyzed in this study represents one of the most widely used materials in MAM, due to its weldability and good properties of casting [10]. Its excellent mechanical, physical and thermal properties, combined with low weight, make it a material of strong interest for applications that require high properties-to-weight ratio, such in the automotive and aerospace industries [10]. The properties of such LPBF-ed alloy have already been studied in the literature, but these studies have focused more on the influence of process parameters on microstructure, internal defect generation and thus on the mechanical performance of AlSi$_{10}$Mg artifacts [11, 12]. Only recently some literature papers have been interested in the tribological aspects of the AlSi$_{10}$Mg alloy, going to study its friction and wear performance, performing tribological tests, such as linear reciprocating or pin/ball on disc ones [13, 14]. It follows that to date, tribological characterization of AM specimens is still an under-explored topic, worthy of much more in-depth investigation.

Therefore, the present study aims to elucidate the tribological performance of LPBF-ed manufactured AlSi$_{10}$Mg alloy products with optimized parameters, characterized by means of progressive load scratch tests and ball on plate wear tests, to evaluate both global and local tribo-technological properties, in order to compare them to as-cast AlSi$_{10}$Mg specimens, as well as to identify also any possible variations induced by the building orientation.

2. MATERIALS AND METHODS

2.1. PRELIMINARY EXPERIMENTAL ACTIVITIES

The material adopted for the LPBF process is a commercial pre-alloyed powder of $AlSi_{10}Mg$ (supplied by m4p Materials Solutions GmbH, Magdeburg, Germany), whose main characteristics, together with the chemical composition, are reported in a previous work [15].

The commercial Additive Manufacturing machine SLM 280HL (by SLM Solutions Group AG, Lübeck, Germany) was used to print the samples tribo-mechanically tested in this work, whose geometry and dimensions are reported in Figure 1 (Left). Also, the main parameters of the AM machine are reported in [15].

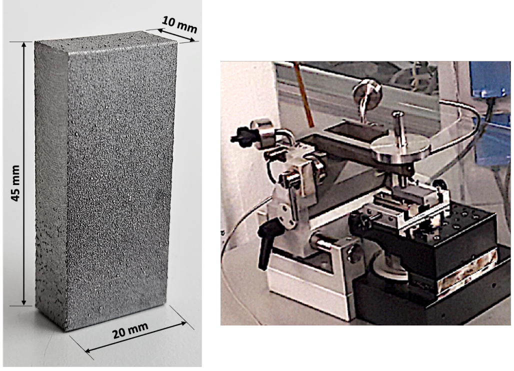

FIGURE 1. (Left) Geometry and dimensions of $AlSi_{10}Mg$ specimens for tribo-technological characterization. (Right) Experimental setup for dry sliding ball-on-plate tests.

In a previous study [15], three Building Orientations (*BO*s) were investigated, i.e., horizontal (0°), vertical (90°), and tilted (45°), as well as two combinations of processing parameters ($C\#$), based on different layer thickness and laser scan speed, as shown in Table 1.

Three samples were tested for each experimental scenario. The operational parameters were fixed according to manufacturer's suggestion, in order to produce full-dense samples. Post-processing processes, conducted for each specimen family, involved only: (i) a wire electrical discharge machining cutting process; (ii) a T6 heat treatment (at 500 °C, for 30 min).

Operational parameters	Values			Units
Building orientation BO	0	45	90	°
Control factors $C\#$	1	2		-
Layer thickness Th	30	50		μm
Laser scan speed Ss	1650	930		mm/s
Laser power P		350		W
Hatch distance Hd		100		μm
Laser beam focus diameter D		80		μm

TABLE 1. Operational parameters and their levels: 3 *BO*s × 2 $C\#$ = 6 experimental conditions.

In previous works, the relative density was quantitatively measured on five different cross-sections for each experimental sample, analyzing the images acquired by means of a 3D laser microscope (LEXT OLS4100, by Olympus Europa SE & Co. KG, Hamburg, Germany) by using Image J software. The full methodology is reported in a previous paper [10]. In addition, the surface roughness was investigated using the high-resolution 3D surface profiling system CLI 2000 by Talysurf (Taylor Hobson, Leicester, UK), according to the standard ISO 25178, acquiring the arithmetical mean and maximum heights of the profile (i.e., Ra and Rz) on $3 \times 3\,\mathrm{mm}^2$ square areas, as reported in [15]. Finally, preliminary tests were conducted to evaluate the UTS (Ultimate Tensile Strength), by using Zwick-Roell testing machine (z010, by Zwick GmbH & Co., Ulm, Germany) on tensile samples, whose geometry was fixed according to the ASTME8/E8M standard, as reported in [10]. Based on these findings from previous works in the literature, it was possible to determine the best scenario (i.e., the best combination of control factors and building orientation), on which specimens to conduct both global and local tribological tests, i.e., scratch and wear tests, in order to also verify possible anisotropic behavior of the specimens, i.e., an effect of the test area on the measured properties.

2.2. TRIBO-TECHNOLOGICAL CHARACTERIZATION

The tribo-technological study was conducted through two different types of tests: (i) ball-on-plate tests in dry sliding configuration, to evaluate the local and global wear properties; (ii) progressive scratch tests with two different diamond indenters, to evaluate local and global scratch properties. Wear tests were conducted using the ball-on-plate test Tribometer by CSM Instruments (Peseux, Switzerland), in non-lubricated mode, at ambient temperature ($\sim 25\,°\mathrm{C}$), as reported in Figure 1 (Right). The following parameters were set: ceramic alumina Al_2O_3 ball (6 mm diameter) as counterpart; 2 N of applied load (i.e., normal force); 5 mm of sliding distance for a total distance of 100 m; 30 Hz of data acquisition frequency; $50\,\mathrm{mm\,s^{-1}}$ of translation speed; $10\,\mathrm{mm\,rev^{-1}}$ of rotation speed. The following were acquired during the tests: coefficient of friction as a function of traveled distance or number of cycles; average coefficient of friction over time. In addition, the specimens were carefully weighed both before and after the test, so as to estimate the material removed during the test. Scratch tests were instead conducted using the Micro Scratch Tester by CSM Instruments (Peseux, Switzerland), in progressive load mode, i.e., with a progressively increasing load from 0.03 N to 30 N, at ambient temperature ($\sim 25\,°\mathrm{C}$). The test involves the succession of 3 phases [16]: (i) profiling of the starting surface (low load, pre-scan); (ii) penetration (scan), recording the normal (N) and the tangential (T) forces, as well as the penetration depth (Pd); (iii) profiling of the tested surface after elastic recovery, so as to measure the residual depth (Rd) (low load, post-scan).

The following parameters were set: 3 mm of track length; a loading rate of $\sim 20\,\mathrm{N\,min^{-1}}$; $2\,\mathrm{mm\,min^{-1}}$ of speed (during scan phase). Two different rounded conical Rockwell C diamond indenters, i.e., with a tip diameter (ϕ) of 100 and $200\,\mu\mathrm{m}$, respectively, were used in order to perform a local characterization of scratch resistance, from which to also derive a global average behavior. As reported in Figure 2, three different areas were examined for both types of tests, i.e., one scratch and one wear trace were produced in the central area, while two more were traced in the side areas, placed about 11 mm from the central trace, to evaluate also the effect of the distance from the support structure during the manufacturing process. So, three equally spaced scratch and wear traces were produced on each sample, testing three different areas (i.e., one trace for each).

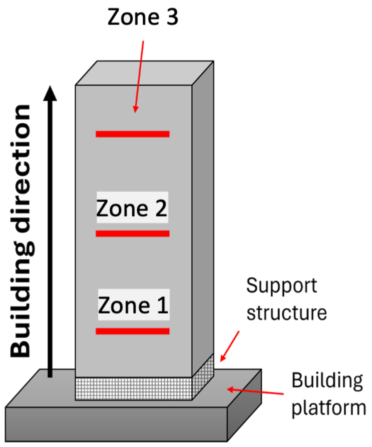

FIGURE 2. Examined zones of the $\mathrm{AlSi_{10}Mg}$ alloy specimens (please note that the figure refers to a specimen produced with a BO of 90°).

3. RESULTS AND DISCUSSION

3.1. RESULTS OF PRELIMINARY INVESTIGATION

Table 2 reports the results with respect to preliminary analyses reported in previous literature papers, used in order to determine the family of specimens with superior mechanical and morphological performance, on which to conduct both global and local tribological tests, i.e., scratch and wear tests.

Preliminary results reported in a previous work [15] showed that specimens grown in a 90° orientation ensured the lowest porosity, specifically achieving the highest mean density of about 93.77 % for the $C\#2$ combination. Comparison with a gravity cast produced foundry specimen, however, showed a significant difference in relative density, attributable to widespread porosity within and on the surface of the material.

At the same time, specimens produced according to $C\#2$ combination showed the lowest roughness values, although significantly higher than $\mathrm{AlSi_{10}Mg}$ specimens produced by Hot Pressing Die Casting (HPDC) [10].

Finally, the analysis of UTS results showed that the combination of $C\#2$ parameters with 90° growth direction ensures the maximum UTS (i.e., 377 ± 30 MPa), higher compared to traditional manufacturing processes (i.e., 333 ± 33 MPa) [10]. By virtue of these considerations, it appears evident that $C\#2$ samples (i.e., $Th = 50\,\mu\mathrm{m}$, $Ss = 0.93\,\mathrm{m\,s^{-1}}$) with $BO = 90°$ offer the best mechanical and morphological performances. Local tribological tests, i.e., scratch and wear tests, were then conducted on that family of specimens to study the effect of the test area on the above properties. From which tests it was also possible to derive a global average behavior of the specimens.

3.2. RESULTS OF TRIBO-TECHNOLOGICAL INVESTIGATION

Figure 3 reports the summary of results about wear tests, i.e., ball-on-plate tests, conducted in dry sliding configuration.

It is pointed out that, in agreement with [14, 15], it was decided to remove, from the calculation of the average and standard deviation values, the measurements of the friction coefficients acquired in the first 20 m of sliding distance, i.e., in the first 650 s of testing. Therefore, the running-in phase of the material, in which the values of the friction coefficients are much higher than in the subsequent steady-state phase, was not considered, because of an initial contact limited only to the asperities of the surfaces of the tested specimen and the ceramic counterpart.

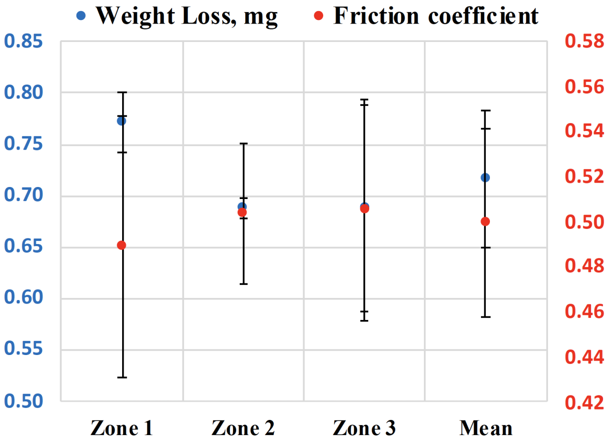

FIGURE 3. Average and standard deviations (SD) values of weight loss and mean friction coefficient for each of the three zones examined. Please note that three trials were conducted for each zone (i.e., one for each of three samples).

It is worth noting how in the first zone the mean friction coefficient is lower than in the other ones, underlining a worse layer adhesion, so a lower tangential force needed to trigger the layer cracking and delamination mechanisms, according to [13, 17].

Properties	LPBF – $C\#1$			LPBF - $C\#2$			HPDC
	0°	45°	90°	0°	45°	90°	
Relative density, %	82.93 ± 8.92	86.18 ± 8.99	93.36 ± 2.78	83.47 ± 7.19	87.72 ± 7.28	93.77 ± 4.87	99.5 ± 0.30 ⋆
UTS, MPa	253 ± 57	309 ± 20	321 ± 30	333 ± 33	357 ± 26	377 ± 30	333 ± 33
Ra, μm	8.52 ± 2.78	9.69 ± 3.32	10.33 ± 3.60	3.18 ± 0.63	3.27 ± 0.60	4.12 ± 0.74	1.8 ± 1.4
Rz, μm	44.8 ± 13.3	51.4 ± 12.0	52.2 ± 15.2	20.8 ± 4.0	22.0 ± 4.3	24.8 ± 4.1	-

⋆ value for gravity cast production [14].

TABLE 2. Comparison of the morphological and mechanical properties between different families of LPBF samples and traditional HPDC ones.

These phenomena are therefore more significant in the first zone, the greater magnitude of which consequently results in a higher weight loss in the zone closer to the support structure, as well shown in Figure 3, and an anisotropic behavior of the AlSi$_{10}$Mg alloy, in agreement with [18].

Globally, however, we show an average weight loss value of $\sim 0.716\,$mg, with an average wear rate (calculated according to [14]) of $\sim 1.429 \cdot 10^{-3}\,\mathrm{mm}^3\,(\mathrm{Nm})^{-1}$ and an average coefficient of friction of ~ 0.499. In agreement with previous literature papers [13, 14], the wear rate is higher than with foundry specimens, under the same load and test distance, as well as the friction coefficient is higher, being affected on the one hand by the porosity of the material, according to [15, 17], which facilitates the mentioned phenomena of layer cracking and delamination, and on the other hand by the different and heterogeneous contact conditions, according to [17], due to the presence of overlapping layers of material by additive means, rather than with a solid foundry specimen.

To confirm the previously reported indications about the anisotropic behavior of the LPBF-ed AlSi$_{10}$Mg material, local scratch resistance tests were conducted, as operated in [9, 19]. As reported in Section 2.2, profiles were first measured for the three test specimens of the $C\#2 - 90°$ family, for the three test zones, the trends of which are shown in Figure 4. For the sake of clarity of the figures and brevity of discussion, only the trends with respect to the first specimen of the family and not of the other two experimental replications will be shown.

It can be seen that the profiles are highly irregular and rough, confirming what was already verified in Section 3.1. In addition, it is shown that internal and surface porosity of the material and the presence of impurities (please refer to Figure 5) are additional causes of high experimental variability.

Figure 6 and 7 show the trends of penetration and residual depths, respectively, for the three zones tested, as well as of the coefficient of friction, for tests conducted with a rounded conical Rockwell C diamond indenter, with a tip radius of $100\,\mu$m.

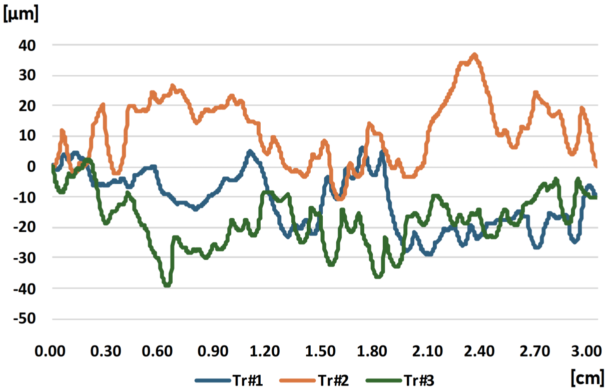

FIGURE 4. Profiles of the three examined test zones ($Tr\#$), for sample #1.

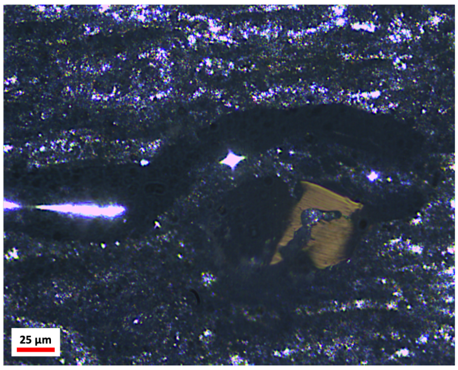

FIGURE 5. Optical micro-graph of an impurity internal to the AlSi$_{10}$Mg alloy (20 × objective).

The results show an absence of linearity for both depths (i.e., Pd and Rd), due to roughness effect (or to an irregular surface), porosity effect (which could lead to major material removal), and presence of impurities (or to a local material variation). It is worth noting the presence of a final pile-up for the tests conducted in each zone (i.e., Rd negative), emphasizing a consistent material springback. The coefficient of friction increases over time due to increased penetration into the material, resulting in a change in the contact conditions during the test, which from being

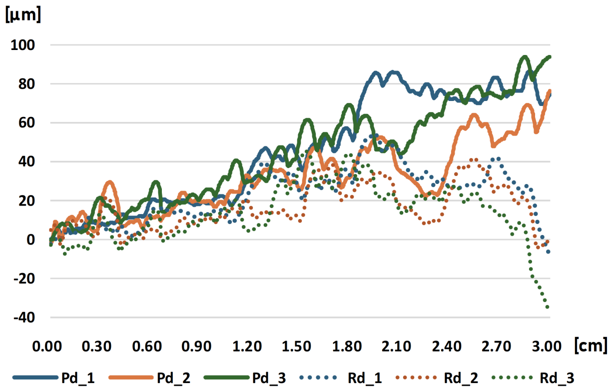

Figure 6. Penetration and residual depths for progressive scratch tests, conducted with a 100 μm tip radius diamond indenter, for sample #1.

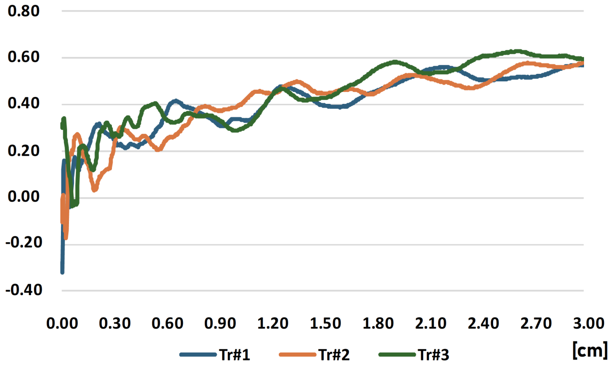

Figure 7. Friction coefficient for progressive scratch tests, conducted with a 100 μm tip radius diamond indenter, for sample #1.

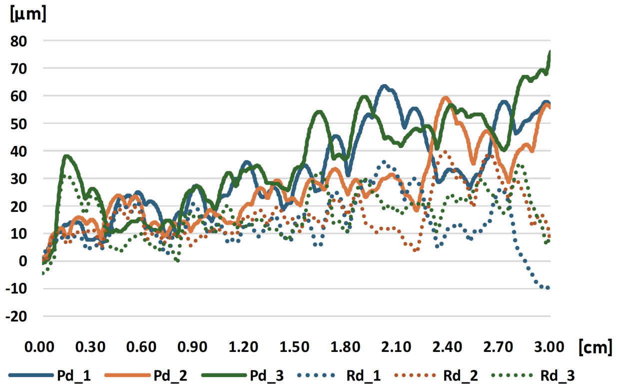

Figure 8. Penetration and residual depths for progressive scratch tests, conducted with a 200 μm tip radius diamond indenter, for sample #1.

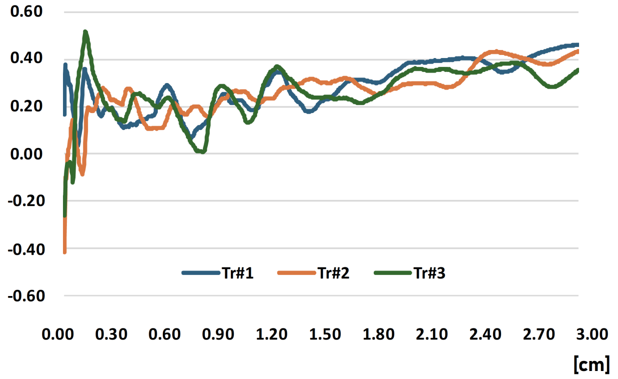

Figure 9. Friction coefficient for progressive scratch tests, conducted with a 200 μm tip radius diamond indenter, for sample #1.

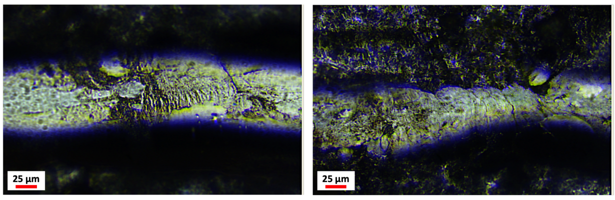

Figure 10. Optical micro-graphs of scratch tracks (20 × objective).

nearly point-like on a smooth surface, gradually becomes more extensive over multiple layers of additive material, resulting in an increase in the relative creep force between the two bodies, i.e., friction [15].

Instead, Figure 8 and 9 show the trends of penetration and residual depths, respectively, for the three zones tested, as well as of the friction coefficient, for tests conducted with a Rockwell C diamond indenter, with 200 μm tip radius. The results show a *Pd* trend similar to that obtained for the 100 μm tip; however, the friction coefficient is significantly lower, highlighting the different morphological contact conditions (i.e., for the same applied normal force, creep is less severe). From the micrographs in Figure 10, an S-shaped rather than linear path of the tip during the scan phase can be seen, due to the effect of internal porosity and the presence of impurities. The images show the presence of cracking zones in the material due to the passage of the tip, with cracking propagation and material layer delamination.

Finally, Figure 11 shows the averages and SDs of mean penetration depth and friction coefficient, as the test zone and indenter tip vary. It is emphasized how, in contrast to the wear tests, in the computation of the average and SD values of mean friction coefficient, all acquired measurements were used, since a steady-state condition does not seem to be reached (i.e., the friction coefficient increases progressively on average during the test). In addition, the initial phase of the test, in which the friction coefficient varies significantly, is very short, i.e., occurring for only the first tenths of a millimeter of test distance, for both tips analyzed, thus not significantly affecting the calculated average and SD values.

The results for *Pd* show that zone 2, i.e., the middle of the specimen, is characterized by more ductile behavior, due to a different thermal cycle, which is slower than the outer zones, in agreement with [15]. This results in a reduction of cracking and delamination, i.e., higher resistance to scratch test for both diamond indenters, highlighting an anisotropic behavior of the material, due

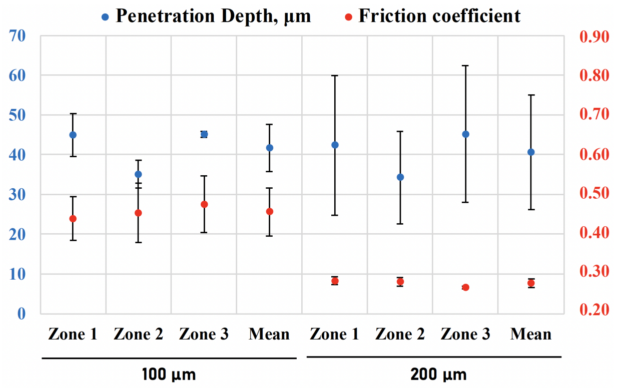

Figure 11. Average and SD values of mean penetration depth and friction coefficient for each of the three zones examined. Please note that three trials were conducted for each zone (i.e., one for each of three samples).

to a layer-by-layer building, in agreement with [18, 19].

While, about the mean friction coefficient, it is really influenced by the indenter geometry, which causes different test severity and creep resistance. The effect of the tip geometry is indeed little in terms of mean *Pd*, whose average value drops from $\sim 41.74\,\mu$m for $100\,\mu$m tip, to $\sim 40.60\,\mu$m for $200\,\mu$m tip; while it causes a substantial reduction in the mean friction coefficient, from ~ 0.456 to ~ 0.276.

4. Conclusions

This work deals with a tribo-technological study to assess global and local features of Laser Powder Bed Fused specimens. In the following the main conclusions:

- based on preliminary results, LPBF-ed samples with a $50\,\mu$m thickness of the powder layer, laser scan speed of $930\,\mathrm{mm\,s^{-1}}$ and 90° building orientation, provide the best tensile response, the lowest porosity and a good surface finishing;
- progressive load scratch and dry ball-on-plate tests show an anisotropic behavior of the material, with higher resistance of the central areas, due to slower cooling that allows to generate more ductile structures (mean *Pd* is $\sim 21.9\,\%$ lower);
- no significant differences are shown in terms of scratch resistance as the indenter changes, while the mean friction coefficient is $\sim 39.4\,\%$ lower, due to different morphological contact conditions;
- finally, wear tests show an overall behavior in terms of dry wear resistance still far from as-cast specimens, with higher wear rate and friction coefficient.

Possible future developments of the work here presented concern the possibility of expanding both the metal alloys analyzed, studying other materials of strong interest in AM, such as 316L stainless steel, and the MAM technologies studied to include other types, such as Selective Laser Sintering, Electron Beam Melting, and Directed Energy Deposition. Through a cross-sectional analysis at the level of MAM materials and technologies, it would be in fact possible to produce tribo-technological optimization proposals also depending on the Additive Manufacturing technology, based on the specific alloys selectable for a given application.

References

[1] I. Yadroitsev, I. Yadroitsava, A. Du Plessis. Basics of laser powder bed fusion. In *Fundamentals of Laser Powder Bed Fusion of Metals*, p. 15–38. Elsevier, 2021. `https://doi.org/10.1016/b978-0-12-824090-8.00024-x`

[2] C. Cai, K. Zhou. Metal additive manufacturing. In *Digital Manufacturing*, p. 247–298. Elsevier, 2022. `https://doi.org/10.1016/b978-0-323-95062-6.00005-x`

[3] C. Yan, Y. Shi, Z. Li, et al. Typical applications of selective laser sintering technology. In *Selective Laser Sintering Additive Manufacturing Technology*, p. 873–932. Elsevier, 2021. `https://doi.org/10.1016/b978-0-08-102993-0.00007-2`

[4] M. Mehrpouya, A. Vosooghnia, A. Dehghanghadikolaei, B. Fotovvati. The benefits of additive manufacturing for sustainable design and production. In *Sustainable Manufacturing*, p. 29–59. Elsevier, 2021. `https://doi.org/10.1016/b978-0-12-818115-7.00009-2`

[5] G. S. Ponticelli, F. Tagliaferri, S. Venettacci, et al. Re-engineering of an impeller for submersible electric pump to be produced by selective laser melting. *Applied Sciences* **11**(16):7375, 2021. `https://doi.org/10.3390/app11167375`

[6] M. Armstrong, H. Mehrabi, N. Naveed. An overview of modern metal additive manufacturing technology. *Journal of Manufacturing Processes* **84**:1001–1029, 2022. `https://doi.org/10.1016/j.jmapro.2022.10.060`

[7] R. K. Upadhyay, A. Kumar. Scratch and wear resistance of additive manufactured 316L stainless steel sample fabricated by laser powder bed fusion technique. *Wear* **458–459**:203437, 2020. `https://doi.org/10.1016/j.wear.2020.203437`

[8] U. Tradowsky, J. White, R. M. Ward, et al. Selective laser melting of $\mathrm{AlSi_{10}Mg}$: Influence of post-processing on the microstructural and tensile properties development. *Materials & Design* **105**:212–222, 2016. `https://doi.org/10.1016/j.matdes.2016.05.066`

[9] Y. Yang, X. Li, M. M. Khonsari, et al. On enhancing surface wear resistance via rotating grains during selective laser melting. *Additive Manufacturing* **36**:101583, 2020. `https://doi.org/10.1016/j.addma.2020.101583`

[10] G. S. Ponticelli, O. Giannini, S. Guarino, M. Horn. An optimal fuzzy decision-making approach for laser powder bed fusion of $\mathrm{AlSi_{10}Mg}$ alloy. *Journal of Manufacturing Processes* **58**:712–723, 2020. `https://doi.org/10.1016/j.jmapro.2020.08.054`

[11] W. H. Kan, Y. Nadot, M. Foley, et al. Factors that affect the properties of additively-manufactured $AlSi_{10}Mg$: Porosity versus microstructure. *Additive Manufacturing* **29**:100805, 2019. `https://doi.org/10.1016/j.addma.2019.100805`

[12] Z. W. Xu, Q. Wang, X. S. Wang, et al. High cycle fatigue performance of $AlSi_{10}Mg$ alloy produced by selective laser melting. *Mechanics of Materials* **148**:103499, 2020. `https://doi.org/10.1016/j.mechmat.2020.103499`

[13] H. Wu, Y. Ren, J. Ren, et al. Effect of melting modes on microstructure and tribological properties of selective laser melted $AlSi_{10}Mg$ alloy. *Virtual and Physical Prototyping* **15**(sup1):570–582, 2020. `https://doi.org/10.1080/17452759.2020.1811932`

[14] P. Tonolini, L. Montesano, M. Tocci, et al. Wear behavior of $AlSi_{10}Mg$ alloy produced by laser-based powder bed fusion and gravity casting. *Advanced Engineering Materials* **23**(10):2100147, 2021. `https://doi.org/10.1002/adem.202100147`

[15] S. Venettacci, G. S. Ponticelli, D. Guarino, S. Guarino. Tribological properties of laser powder bed fused $AlSi_{10}Mg$: Experimental study and statistical analysis. *Journal of Manufacturing Processes* **84**:1103–1121, 2022. `https://doi.org/10.1016/j.jmapro.2022.10.065`

[16] M. Barletta, F. Trovalusci, A. Gisario, S. Venettacci. New ways to the manufacturing of pigmented multi-layer protective coatings. *Surface and Coatings Technology* **232**:860–867, 2013. `https://doi.org/10.1016/j.surfcoat.2013.06.113`

[17] W. H. Kan, S. Huang, Z. Man, et al. Effect of T6 treatment on additively-manufactured $AlSi_{10}Mg$ sliding against ceramic and steel. *Wear* **482–483**:203961, 2021. `https://doi.org/10.1016/j.wear.2021.203961`

[18] A. K. Mishra, R. K. Upadhyay, A. Kumar. Surface wear anisotropy in $AlSi_{10}Mg$ alloy sample fabricated by selective laser melting: Effect of hatch style, scan rotation and use of fresh and recycled powder. *Journal of Tribology* **143**(2):021701, 2020. `https://doi.org/10.1115/1.4047788`

[19] Y. Yang, Y. Zhu, M. M. Khonsari, H. Yang. Wear anisotropy of selective laser melted 316L stainless steel. *Wear* **428–429**:376–386, 2019. `https://doi.org/10.1016/j.wear.2019.04.001`